Airborne Laser Scanning for Corridor Mapping: Georeferencing with Tightly-coupled Multi-view LiDAR

Florian Pöppl[a], Andrea Spitzer[a], Andreas Ullrich[a], Norbert Pfeifer[b]

[a]RIEGL Laser Measurement Systems GmbH – (fpoeppl, aspitzer, aullrich)@riegl.com
[b]Technische Universität Wien – norbert.pfeifer@geo.tuwien.ac.at

Keywords: Direct georeferencing, 3D mapping, sensor orientation, trajectory estimation

Abstract

Airborne laser scanning enables efficient acquisition of 3D point clouds, particularly in corridor mapping applications. This article presents a georeferencing workflow which integrates GNSS, and IMU and LiDAR data within a non-linear least-squares adjustment framework. Corridor mapping poses difficulties for navigation and georeferencing due to the lack of turns or other dynamics, which leads to drift in the estimated trajectory, especially the aircraft heading. The use of strip adjustment or similar techniques is standard in airborne laser scanning, but the benefits are limited in corridor mapping as point cloud overlap is intentionally minimized in order to maximize ground covered in a given time frame. The proposed georeferencing approach aims to improve georeferencing in two ways: (1) tight coupling of IMU and LiDAR data allows for better in-run estimation of IMU errors and thereby improves the overall accuracy of trajectory and georeferenced point cloud, and (2) the use of a multi-view laser scanner effectively creates point cloud overlap within a single pass of the corridor by scanning in three distinct viewing directions (nadir, forward, backward). This georeferencing approach is presented and applied to power line corridor mapping, specifically an airborne laser scanning dataset acquired with a helicopter, and is evaluated based on trajectory and point cloud. The results show that the use of multi-view LiDAR within the trajectory estimation mitigates heading drift even with only a single pass of the corridor.

1. Introduction

Airborne laser scanning, where the laser scanner is mounted on a airplane or helicopter, allows for large-scale acquisition of 3D data, specifically point clouds. The laser scanner uses light detection and ranging (LiDAR) to measure the range to a target, while varying and measuring the deflection of the laser beam. The measurements, initially available as polar coordinates (range and one or two angles) must be transformed first into Cartesian coordinates relative to the scanner itself and then to a georeferenced coordinate system. This requires knowledge of the platforms' trajectory (its position and orientation over time) and thus necessitates integration with auxiliary navigation systems. In particular, typical airborne laser scanning systems comprise a global navigation satellite system (GNSS) receiver and antenna, and an inertial measurement unit (IMU). The combination of satellite and inertial navigation is advantageous, as the former provides absolute positioning at a low frequency and the latter provides relative position and orientation at a higher frequency. However, inertial sensors suffer from time-varying measurement errors that cause a stand-alone inertial navigation solution to drift over time. When combining inertial measurements with other sources of position and orientation information, typically positions from GNSS, these errors may be calibrated for in-run. However, the trajectory resulting from fusion of GNSS and IMU data still contains errors, which manifest as discrepancies in the point cloud data if the same area is scanned multiple times and from multiple locations. These discrepancies can be minimized in a strip adjustment (Glira et al., 2015; Jonassen et al., 2023). A common processing workflow in airborne laser scanning is thus comprised of two steps, (1) estimating a trajectory from GNSS/IMU data, and (2) improving trajectory and possibly system calibration in a strip adjustment. Recent holistic approaches integrate GNSS, IMU and LiDAR data into one non-linear least-squares (NLS) adjustment (Brun et al., 2022; Pöppl et al., 2024), possibly together with image data (Mouzakidou et al., 2024). These approaches are similar to some graph-based simultaneous localization and mapping (SLAM) methods popular in robotics (Cadena et al., 2016), but are developed with focus on airborne mapping applications and the quality of the resulting georeferenced mapping product.

In *corridor mapping*, data acquisitions are typically performed in one or both directions along the corridor and with minimal overlap to maximize efficiency when mapping e.g., railways or power lines (Huang et al., 2021; Munir et al., 2023). This poses additional difficulty for navigation and georeferencing. The orientation derived from fusion of GNSS and IMU data can start to drift over longer flight periods at constant velocity without changes in flight direction. Specific re-initialization maneuvers may be required to allow accurately estimating gyroscope biases and consequently the orientation, especially the aircraft heading. However, this is often difficult to efficiently and economically integrate into a given flight plan. In holistic GNSS/IMU/LiDAR processing approaches, the *tight-coupling* of IMU and LiDAR allows compensating for IMU drift because the position and orientation constraints derived from overlaps in the LiDAR data help estimate IMU biases and scale factors more accurately than when only using position information from GNSS. Both conventional strip adjustment approaches and holistic GNSS/IMU/LiDAR processing approaches require overlaps in the acquired point clouds, yet overlap is undesirable in corridor mapping as any overlap decreases acquisition efficiency and increases flight time as the same area has to be flow over several times.

In this article, we employ a laser scanner with a *multi-view* scan geometry which scans nadir, forward and backward (NFB) and thus creates overlapping point clouds within a single flight strip, without revisiting the same area. While some in-strip overlap is also obtained from e.g., circular scan patterns, the focus is here

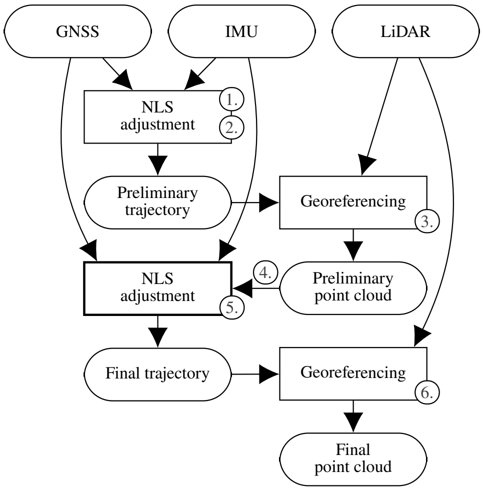

Figure 1. Trajectory Estimation and Georeferencing workflow from Pöppl et al. (2025).

on the three distinct viewing directions and the application to corridor mapping. We describe the method and results of a holistic trajectory estimation and georeferencing approach (Fig. 1) applied to helicopter-based power line mapping, and thereby investigate and evaluate the possible benefits of multi-view LiDAR in the context of georeferencing in such a use-case.

Section 2 introduces the processing workflow and underlying algorithms with focus on multi-view LiDAR. Section 3 presents the acquired and processed data and evaluates the results by comparing trajectory and point cloud from different processing runs and with respect to reference data on the ground. Section 4 concludes with a short summary and outlook.

2. Georeferencing with Tightly-Coupled LiDAR

The full georeferencing workflow (Fig. 1) used here consists of (1) filter-based initialization, (2) GNSS/IMU adjustment, (3) preliminary georeferencing, (4) planar feature extraction and matching, (5) GNSS/IMU/LiDAR adjustment, and (6) final georeferencing, resulting in the final point cloud. The second adjustment (step 5) includes GNSS positions and IMU measurements as well as observations derived from corresponding planes extracted from the LiDAR data, and thus represents a tight coupling of IMU and LiDAR. This normally requires significant overlap in the flight strips. Here, a *RIEGL* VUX-160[23] laser scanner is used, which features a multi-view scan geometry with three distinct directions: nadir, 10° forward, 10° backward (NFB, Fig. 2). This makes it especially suitable for corridor mapping, as the NFB scanning reduces scan shadows and creates overlap even within a single flight strip (i.e., a single pass of the corridor), allowing the LiDAR-derived plane observations to function as short-term position and orientation constraints even if there is no overlap from neighbouring flight strips.

Below follows a short overview of the estimation method itself and the relevant measurement equations (GNSS positions, IMU angular velocity and specific force, and LiDAR-derived plane correspondences). For details the reader is referred to the in-depth description in previous work (Pöppl et al. (2023b, 2024, 2025), on which the following description is loosely based. The GNSS, IMU and LiDAR sensor fusion, which integrates all available data in a non-linear least-squares (NLS) adjustment, forms the core of the georeferencing workflow. This NLS adjustment is based on explicit functional models for all observation types: GNSS positions, IMU angular velocity and specific force, and LiDAR-derived plane correspondences. In general, for n noisy vector-valued measurements $\widetilde{\boldsymbol{y}}_i$ of true values $\boldsymbol{y}_i$, the true values are modelled as a function of unknown parameters $\boldsymbol{x}$, so that $\boldsymbol{y}_i := f_i(\boldsymbol{x})$ and the measurements $\widetilde{\boldsymbol{y}}_i$ are the sum of model and additive noise

Figure 2. *RIEGL* VUX-160[23] nadir/forward/backward (NFB) scan directions and field of view.

$$\begin{aligned} \underbrace{\widetilde{\boldsymbol{y}}_i}_{\text{measurement}} &:= \boldsymbol{y}_i + \boldsymbol{\epsilon}_i \\ &= \underbrace{f_i(\boldsymbol{x})}_{\text{model}} + \underbrace{\boldsymbol{\epsilon}_i}_{\text{noise}} . \end{aligned} \tag{1}$$

The errors $\boldsymbol{\epsilon}_i$ are assumed to be Gaussian, with zero mean, variance $\boldsymbol{\Sigma}_i$, and uncorrelated between different measurements. The least-squares estimate is given by

$$\boldsymbol{x}^* = \underset{\boldsymbol{x}}{\operatorname{argmin}} \sum_i (f_i(\boldsymbol{x}) - \widetilde{\boldsymbol{y}}_i)^T \boldsymbol{\Sigma}_i^{-1} (f_i(\boldsymbol{x}) - \widetilde{\boldsymbol{y}}_i), \tag{2}$$

or a robustified variation (e.g., using Huber loss) thereof. This minimization problem can be solved by standard non-linear optimization techniques, in this case using the Levenberg-Marquardt algorithm. This requires suitable starting values for all parameters, especially those that occur in highly non-linear equations, i.e., the orientations, obtained by e.g., a simple GNSS/IMU Kalman filter. Solving the optimization problem is an iterative process that involves solving large systems of linear equations at each iteration step, which is computationally expensive for large datasets. A recent extension (Pöppl et al., 2025) addresses scalability by employing an iterated IMU down- and upsampling scheme which reduces the size of the NLS adjustment without negatively impacting accuracy, making this approach applicable to longer and larger datasets. This is achieved by splitting the trajectory into low- and high-frequency parts, where only low-frequency trajectory parameters are estimated within the adjustment using downsampled IMU measurements, and high-frequency dynamics are reconstructed from raw inertial measurements.
All sensors are mounted rigidly on the moving platform, in this case a helicopter. The parameters $\boldsymbol{x}$ to be estimated are: (1) position $\boldsymbol{p}(t)$ and orientation $\boldsymbol{R}(t)$ of the platform, referenced to the IMU itself, and (2) object space parameters modelling the location and orientation of planar surfaces (Pöppl et al., 2024). The GNSS antenna lever arm $\boldsymbol{l}_a$ has been determined previously and is here considered known. The trajectory is modelled using euclidean Hermite splines for position and quaternion Hermite splines for orientation.

Absolute positioning is realized through loosely-coupled GNSS, where the raw GNSS observables are pre-processed into a standalone GNSS position solution that is then integrated with IMU and LiDAR data in the adjustment. This GNSS position refers to the position of the GNSS antenna. Conversely, the GNSS antenna position may be derived from the modelled platform position $\boldsymbol{p}(t)$, the platform orientation $\boldsymbol{R}(t)$ and the GNSS antenna lever arm $\boldsymbol{l}_a$. For a GNSS position measurement $\widetilde{\boldsymbol{p}}$ at time t, the measurement equation is given by

$$\underbrace{\widetilde{\boldsymbol{p}}}_{\text{measurement}} = \underbrace{\boldsymbol{p}(t) + \boldsymbol{R}(t)\,\boldsymbol{l}_a}_{\text{model}} + \underbrace{\boldsymbol{\epsilon}_p}_{\text{noise}}, \tag{3}$$

where the measurement errors $\boldsymbol{\epsilon}_p$ are assumed zero-mean and normally distributed with covariance $\boldsymbol{\Sigma}_p$. An estimate of the measurement covariance is available as output of the GNSS processing. The errors are assumed to be uncorrelated, which is generally not the case in practice; if necessary, the error model may be adapted to account for time-correlation (Pöppl et al., 2023a).

The IMU is composed of a three-axis accelerometer and gyroscope, which provide measurements $\widetilde{\boldsymbol{f}}$ and $\widetilde{\boldsymbol{\omega}}$ of specific force $\boldsymbol{f}$ and angular velocity $\boldsymbol{\omega}$. The measurement model for the inertial measurements is derived from the standard strap-down inertial navigation equations (cf. Groves 2013 and Pöppl et al. 2025). Inertial measurements are assumed to be tainted by additive white noise $\boldsymbol{\epsilon}_\star$, as well as biases $\boldsymbol{b}_\star$ and scale factor errors $\boldsymbol{S}_\star = \operatorname{diag}(s_{x\star}, s_{y\star}, s_{z\star})$. The measurement equation for specific force and angular velocity at a time t is then given by

$$\underbrace{\begin{matrix}\widetilde{\boldsymbol{f}}\\ \widetilde{\boldsymbol{\omega}}\end{matrix}}_{\text{measurement}} \begin{matrix}=\\=\end{matrix} \underbrace{\begin{matrix}(I+\boldsymbol{S}_{\boldsymbol{f}})\,\boldsymbol{f}(t)+\boldsymbol{b}_f(t)\\ (I+\boldsymbol{S}_\omega)\,\boldsymbol{\omega}(t)+\boldsymbol{b}_\omega(t)\end{matrix}}_{\text{model}} \begin{matrix}+\\+\end{matrix} \underbrace{\begin{matrix}\boldsymbol{\epsilon}_f\\ \boldsymbol{\epsilon}_\omega\end{matrix}}_{\text{noise}}. \tag{4}$$

The inertial measurements are modelled explicitly in the adjustment, which allows in-run estimation of biases and scale factor errors. This is already possible when integrating only IMU and GNSS data, but significantly benefits from tightly-coupling with LiDAR data. In this case, the LiDAR-derived observations (see below) improve the estimation of IMU errors and therefore improve overall trajectory accuracy.

If there are errors in the trajectory, these propagate through the georeferencing and cause discrepancies between point clouds in areas which are visible in multiple flight strips or viewing directions. The redundant information in overlapping point clouds is used to constrain the trajectory. Here, planar surfaces are used as features, which are extracted from point clouds (Fig. 3) and matched to other spatially nearby planar features (Pöppl et al., 2023b). All corresponding planar features are aggregated into a planar object, which serves as a model for the physical surface. A planar feature is defined by plane center $\widetilde{\boldsymbol{c}}$ and plane normal $\widetilde{\boldsymbol{n}}$, and may be considered a measurement of the planar object, which is in turn described by a plane center $\boldsymbol{c}$ and plane normal $\boldsymbol{n}$. Under the assumption that these planar features describe the same object, three constraints are formed describing the normal distance between the planes and the slopes of object plane w.r.t. the feature plane axes (Pöppl et al. 2024)

$$\underbrace{\begin{matrix}\boldsymbol{0} = (\boldsymbol{c}-\widetilde{\boldsymbol{c}})\cdot\widetilde{\boldsymbol{n}}\\ \boldsymbol{0} = (\widetilde{\boldsymbol{n}}\cdot\widetilde{\boldsymbol{k}}_1)/(\boldsymbol{n}\cdot\widetilde{\boldsymbol{n}})\\ \boldsymbol{0} = (\widetilde{\boldsymbol{n}}\cdot\widetilde{\boldsymbol{k}}_2)/(\boldsymbol{n}\cdot\widetilde{\boldsymbol{n}})\end{matrix}}_{\text{constraint}} \begin{matrix}+\\+\\+\end{matrix} \underbrace{\begin{matrix}\boldsymbol{\epsilon}_n\\ \boldsymbol{\epsilon}_{k_1}\\ \boldsymbol{\epsilon}_{k_2}\end{matrix}}_{\text{noise}}. \tag{5}$$

The plane axes $\boldsymbol{k}_1, \boldsymbol{k}_2$ (respectively $\widetilde{\boldsymbol{k}}_1, \widetilde{\boldsymbol{k}}_2$) are chosen so that $[\boldsymbol{k}_1\,\boldsymbol{k}_2\,\boldsymbol{n}]$ (respectively $[\widetilde{\boldsymbol{k}}_1\,\widetilde{\boldsymbol{k}}_2\,\widetilde{\boldsymbol{n}}]$) are orthonormal, but are otherwise arbitrary. For each object plane, an offset and two slopes are explicitly estimated. Each feature plane is internally stored as center $\widetilde{\boldsymbol{c}}_s$, axes $\widetilde{\boldsymbol{k}}_{s1}, \widetilde{\boldsymbol{k}}_{s2}$ and normal $\widetilde{\boldsymbol{n}}_s$ in the scanner coordinate system. To form the measurement equations in Eq. (5) in object space, the feature plane in scanner coordinate representation is transformed into the required object space coordinates $\widetilde{\boldsymbol{c}}$ and vectors $\widetilde{\boldsymbol{k}}_1, \widetilde{\boldsymbol{k}}_2, \widetilde{\boldsymbol{n}}$ using the georeferencing equation (see Pöppl et al. 2024) and the current estimate of position and orientation. Note that here, correspondences are formed not only between different flight strips with large temporal separation, but also within short time intervals due to the three viewing directions of the laser scanner.

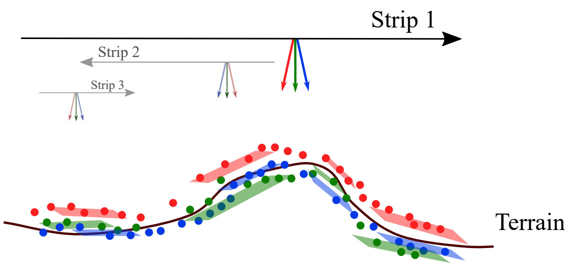

Figure 3. Trajectory errors cause discrepancies in overlapping point clouds originating from different strips or views. Planar features are extracted and then matched with each other.

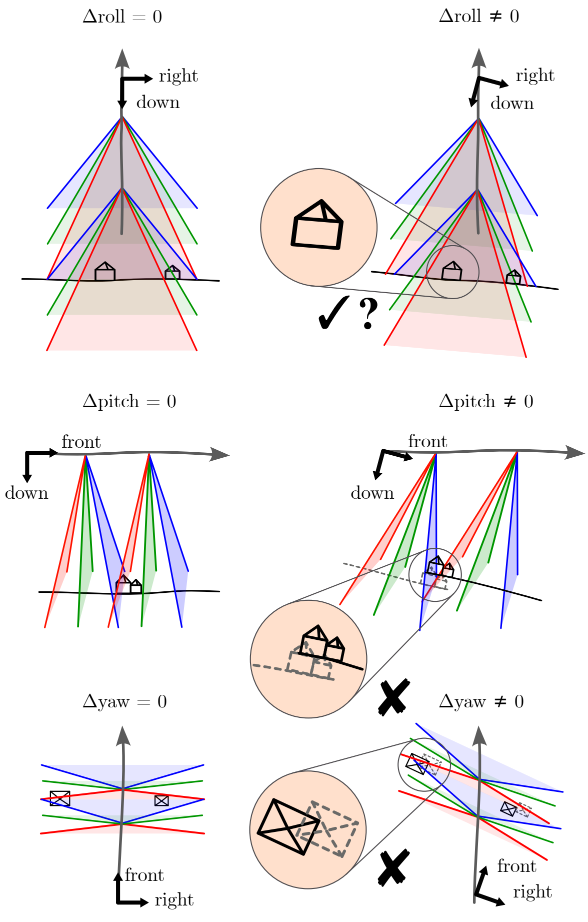

Figure 4. Point cloud discrepancies caused by orientation errors (Δroll, Δpitch, Δyaw) with NFB scanning. The left side shows the NFB scan geometry with no orientation errors, the right side for non-zero roll, pitch or yaw error.

Figure 5. Helicopter platform with *RIEGL* VUX-160[23] laser scanner and RiLOC-E[25] IMU/GNSS navigation system, operated by *Alto Drones*. The second laser scanner is not used.

The point clouds from the three scan directions acquired within a single flight strip (or equivalently a single flight in one direction along the corridor) overlap with certain temporal separation, depending on flying height and aircraft speed. With 10° degrees angle between nadir/forward and nadir/backward directions (Fig. 2), respectively, at a height of 160 m AGL and a velocity of 18 m/s (corresponds to the dataset discussed in Section 3), the forward and nadir direction (and the nadir and backward direction) observe the same object approximately 1.5 seconds apart. However, LiDAR-derived correspondences between the three scan directions not only provide relative constraints at intervals of 1.5 seconds or 3 seconds, but are also expected to mitigate constant orientation offsets (Fig. 4). Pitch and yaw errors cause an apparent mismatch in the point clouds from the different scan directions, and constraints introduced between the different scan directions thus stabilize the estimated aircraft pitch and especially yaw angle. However, a roll error affects all scan direction's points equally and is thus not discernible or correctable given LiDAR data from only a single pass. Another benefit of the non-nadir scan directions is the reduction of scan shadows, especially on vertical surfaces such as building facades. This allows extracting and matching a larger number of vertically oriented planar features (Pöppl et al., 2023a), which are essential in constraining the horizontal position.

3. Application to Corridor Mapping

Corridor mapping using airborne laser scanning (ALS) is often performed for documentation and monitoring of overhead power lines and pylons. The ALS dataset which serves as case study here is acquired in the Eisacktal (Valle Isarco) in South Tyrol, following the power line from Schabs (Sciaves) past Brixen (Bressanone) to Waidbruck (Ponte Gardena). The data acquisition was performed by *Alto Drones GmbH* using a helicopter carrying a *RIEGL* VUX-160[23] laser scanner system with integrated RiLOC-E[25] IMU/GNSS navigation system. All components are mounted on the front of the helicopter Fig. 5. The 30 km section of overhead power line was mapped twice, with one pass once in each direction (north-to-south and south-to-north, see Fig. 6). The flight was performed at 160 m AGL with a ground velocity of 18 m/s and a measurement rate of 1.8 MHz, resulting in an average point density of 150/m^2 (50/m^2 per scan direction) for each direction. The 100° wide field of view of the laser scanner (Fig. 2) results in a strip width of more than 500 m, with lower point densities at the edges.

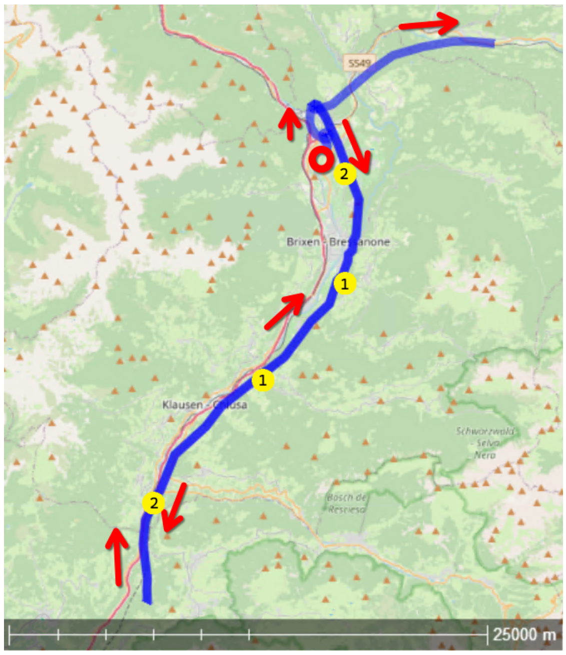

(Map data © OpenStreetMap contributors.)

Figure 6. Data acquisition flight path. The helicopter took off at the airfield marked with a circle and, after a short initialization maneuver, mapped 30 km of overhead power line in two passes. The final portion of the flight, east towards a different airfield, is not used. Reference surfaces (6 surfaces at 4 sites) are marked in yellow.

In addition to the ALS data, reference data was acquired on the ground via standard RTK survey. Along the corridor, 6 horizontal references surfaces (with 4 RTK points each) in 4 sites were measured with an expected accuracy at the centimeter-level, sufficient to allow comparison to the ALS point cloud. Although LiDAR data is integrated into the trajectory estimation, the resulting point clouds are directly georeferenced in the sense that no ground control is used; the reference surfaces are used exclusively for validation.

The ALS data is processed with the aforementioned workflow, and evaluated based on the trajectory and point cloud. Three separate trajectory and point cloud results are compared:

- *Full G/I* trajectory and point cloud: The first part of the processing (steps 1-3 in Fig. 1) result in a trajectory obtained from integration of GNSS and IMU data, and a point cloud georeferenced with that trajectory. Data from the full flight, i.e., both passes of the corridor, is used.
- *Full G/I/L* trajectory and point cloud: After obtaining the initial trajectory and point cloud (steps 1-3), plane correspondences are extracted (step 4), introduced into the adjustment (steps 5), and an improved trajectory is obtained from integration of GNSS, IMU and LiDAR data together with a corresponding georeferenced point cloud (step 6). Data from the full flight, i.e., both passes of the corridor, is used.
- *North-to-South G/I/L* trajectory: Again based on the G/I trajectory and point cloud, LiDAR correspondences are extracted and introduced in the adjustment, resulting in an improved trajectory and point cloud. Only data from the north-to-south pass of the corridor is used. Thus, there is no overlap in the point clouds except that from nadir, forward and backward scan directions.

	Mean (cm)	**RMSE** (cm)	**AVG-SD** (cm)
G/I	-0.36	2.13	1.01
G/I/L	-0.36	2.17	0.33

Table 1. Mean, RMSE and AVG-SD of full G/I and G/I/L point clouds compared to the 6 reference planes. The AVG-SD value refers to the average per-surface standard deviation.

The full G/I/L trajectory is the product of an NLS adjustment using all data from GNSS, IMU and LiDAR and serves as reference trajectory, as no other reference is available. Due to higher redundancy through use of all data and the tight coupling of IMU and LiDAR, it can be expected to be sufficiently accurate for this purpose (cf. Pöppl et al. 2023b, 2024). Additionally, its quality is evaluated based on internal consistency of the resulting point clouds and comparison to reference surfaces on the ground. Fig. 7 shows strip differences for all point clouds in a representative semi-urban area near the northernmost reference surfaces, georeferenced with the GNSS/IMU trajectory (G/I, Fig. 7a) and the GNSS/IMU/LiDAR trajectory (G/I/L, Fig. 7b). The maximum difference between point clouds from the two different passes or different scan directions is at or below 5 cm for planar surfaces (roads, building roofs, etc.). Note that this is only a suitable metric for mostly planar surfaces, and not for vegetated areas. In comparison, the strip differences are notably lower for the GNSS/IMU/LiDAR results, where the optimization minimizes discrepancies between the overlapping point clouds by design. This indicates the G/I/L solution is superior in internal consistency, although no statement about absolute position can be made. For this, the point clouds are compared to the 6 reference surfaces individually and in aggregate (Table 1) by extracting nearby points and computing their distance in normal directions to the reference surfaces. Both solutions show good accuracy, with a mean offset of below 4 mm, and a root mean square error below 22 mm. Each reference surface is observed 3 times for each pass, resulting in a total of 36 observations. As a measure of inter-strip precision, the average standard deviation of observations corresponding to the same reference surface is reported. In this case, average standard deviation of the G/I/L solution is 3.3 mm, a reduction by 2/3 compared to the 10mm of the G/I solution. In summary, the G/I/L solution is more precise and consistent, and at least as accurate, as the G/I solution. In this case, absolute accuracy is determined largely by the GNSS solution which is the same for both G/I and G/I/L results, and the point cloud consistency depends on the accuracy of the orientation. As a consequence, the estimated orientation is expected to be more accurate for the G/I/L solution and hence serves as reference.

The performance of the GNSS/IMU integration (step 2 in Fig. 1) and the benefits of including LiDAR observations derived from single-pass NFB point clouds (step 5 in Fig. 1 but with data from only one pass) are now evaluated by comparing to that reference. Fig. 8 shows as an example a point cloud of power line plus pylon, colored by reflectance and scan direction, respectively. The multiple view directions of NFB scanning are expected to not only reduce scan shadows and increase coverage in the resulting point cloud, but specifically to provide LiDAR-correspondences even for single passes of the corridor, allowing the adjustment to correct pitch and yaw errors (cf. Fig. 4). This is confirmed in Fig. 9, which shows the difference in roll, pitch, and yaw between the full G/I and G/I/L trajectory, and between the north-to-south G/I/L trajectory and full G/I/L trajectory. Compared to that reference, the G/I trajectory exhibits an root mean square

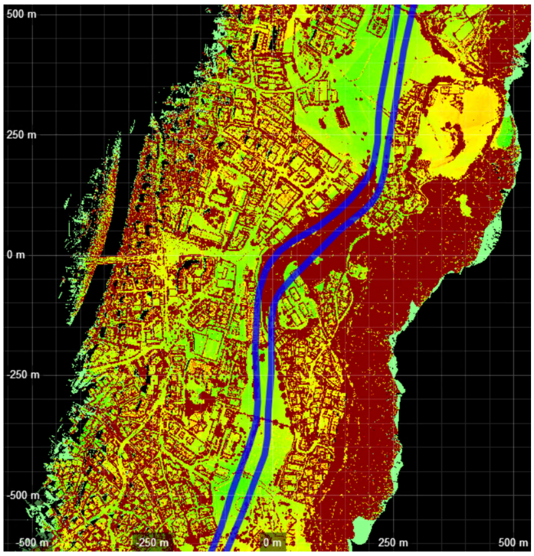

(a) Strip differences for all G/I point clouds (both passes).

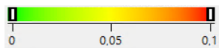

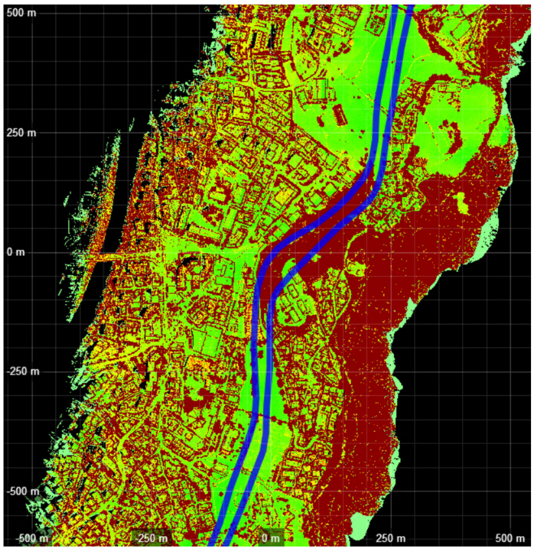

(b) Strip differences for all G/I/L point clouds (both passes).

Figure 7. Strip differences of a semi-urban area near Brixen (Bressanone), computed as maximum minus minimum height, colored from low (0.0 m, green) to high (0.1 m, red). Height is derived from a best-fit plane in a 1 m × 1 m raster cell, separately for each pass and scan direction.

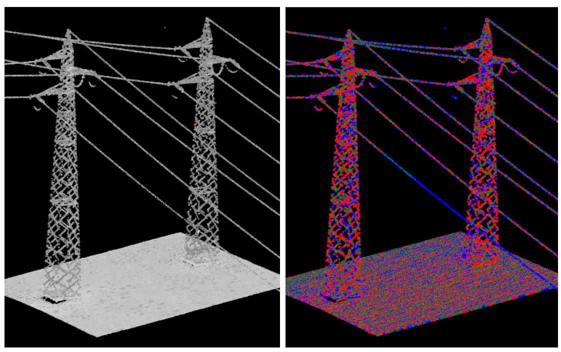

Figure 8. Point cloud of power line and pylon, colored by reflectance (left) and scan direction (right).

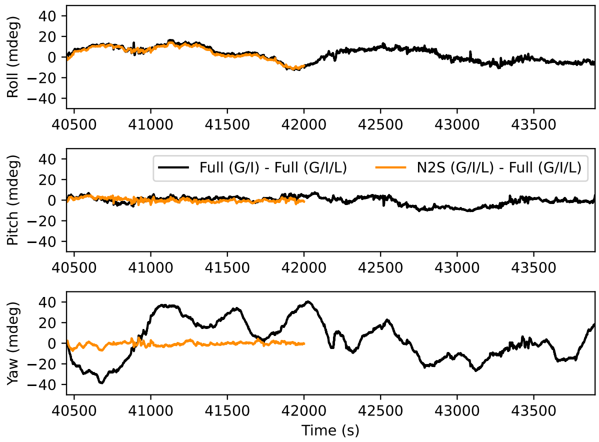

Figure 9. Difference between full G/I trajectory and full G/I/L trajectory, and between north-to-south G/I/L trajectory and full G/I/L trajectory.

error of 8 mdeg for roll, 4 mdeg for pitch, and 20 mdeg for yaw. As argued earlier, a lower accuracy for the heading (yaw) is expected in this case. When comparing the north-to-south G/I/L trajectory to the full G/I/L trajectory, the differences in yaw are reduced drastically, to an RMSE of 2 mdeg. The differences in pitch are also reduced slightly to an RMSE of 2 mdeg, and the differences in roll remain at the same level. This is in agreement with the theoretical considerations (Fig. 4), as a roll error is not apparent given data from only one pass of the corridor. Pitch and yaw error however are apparent, and are thus reduced through integration of LiDAR correspondences derived from the nadir, forward, and backward scan directions. This is especially valuable for the yaw angle, which is difficult to estimate from only GNSS and IMU data in such a setting, whereas the pitch angle is determinable with relatively high accuracy and thus the improvement is limited. The roll angle cannot be improved in this way and roll errors may cause point clouds acquired in a single pass to exhibit a small tilt around the forward axis. In corridor mapping, this might be tolerable as the objects of interest are located in the center of the strip, where roll errors are the least apparent. Nevertheless, to maximize georeferencing accuracy without reducing acquisition efficiency too much, the flight planning could be adapted to include short cross-strips at regular intervals, e.g., every 10 km, to make slowly-varying roll errors observable and thus stabilize roll accuracy in an integrated trajectory estimation.

4. Conclusion

In summary, a holistic trajectory estimation and georeferencing workflow for airborne corridor mapping is proposed, implemented, and analyzed. The tight coupling of IMU and LiDAR in the trajectory estimation results in more precise and consistent point clouds compared to georeferencing with a purely GNSS and IMU derived trajectory. Absolute accuracy is evaluated through comparison to reference planes on the ground, and depends largely on the accuracy of the underlying GNSS solution. The results indicate that the introduction of correspondences from multi-view LiDAR improve trajectory accuracy, especially of the heading angle, even in single passes of the corridor. The possibility to perform accurate corridor mapping with a single pass, possibly with interspaced short cross-strips or loops, increases the efficiency and lowers cost of such data acquisitions.

5. Acknowledgements

We would like to thank Thomas Fontana and Florian Fink from Alto Drones GmbH for expertly and enthusiastically carrying out the ALS data acquisition and on-site RTK survey.

References

Brun, A., Cucci, D. A., Skaloud, J., 2022. LiDAR Point–to–Point Correspondences for Rigorous Registration of Kinematic Scanning in Dynamic Networks. *ISPRS Journal of Photogrammetry and Remote Sensing*, 189, 185–200.

Cadena, C., Carlone, L., Carrillo, H., Latif, Y., Scaramuzza, D., Neira, J., Reid, I., Leonard, J. J., 2016. Past, Present, and Future of Simultaneous Localization And Mapping: Towards the Robust-Perception Age. *IEEE Transactions on Robotics*, 32(6), 1309–1332.

Glira, P., Pfeifer, N., Briese, C., Ressl, C., 2015. A Correspondence Framework for ALS Strip Adjustments Based on Variants of the ICP Algorithm. *Photogrammetrie - Fernerkundung - Geoinformation*, 2015(4), 275–289.

Groves, P. D., 2013. *Principles of GNSS, Inertial, and Multisensor Integrated Navigation Systems*. GNSS Technology and Application Series, 2nd ed. edn, Artech House, Boston.

Huang, Y., Du, Y., Shi, W., 2021. Fast and Accurate Power Line Corridor Survey Using Spatial Line Clustering of Point Cloud. *Remote Sensing*, 13(8), 1571.

Jonassen, V. O., Kjørsvik, N. S., Gjevestad, J. G. O., 2023. Scalable Hybrid Adjustment of Images and LiDAR Point Clouds. *ISPRS Journal of Photogrammetry and Remote Sensing*, 202, 652–662.

Mouzakidou, K., Brun, A., Cucci, D. A., Skaloud, J., 2024. Airborne Sensor Fusion: Expected Accuracy and Behavior of a Concurrent Adjustment. *ISPRS Open Journal of Photogrammetry and Remote Sensing*, 100057.

Munir, N., Awrangjeb, M., Stantic, B., 2023. Power Line Extraction and Reconstruction Methods from Laser Scanning Data: A Literature Review. *Remote Sensing*, 15(4), 973.

Pöppl, F., Pfennigbauer, M., Ullrich, A., Mandlburger, G., Neuner, H., Pfeifer, N., 2023a. Modelling of GNSS Positioning Errors in a GNSS/INS/LiDAR-integrated Georeferencing. *Publikationen Der Deutschen Gesellschaft Für Photogrammetrie, Fernerkundung Und Geoinformation e.V.*, 183–196.

Pöppl, F., Teufelsbauer, H., Ullrich, A., Pfeifer, N., 2023b. Mobile Laser Scanning with Low-Cost Navigation Sensors: Compensating for Low-Grade IMU with Dual-GNSS and Tightly-Coupled LiDAR. *The International Archives of the Photogrammetry, Remote Sensing and Spatial Information Sciences*, XLVIII-1/W1-2023, 403–410.

Pöppl, F., Ullrich, A., Mandlburger, G., Pfeifer, N., 2024. A Flexible Trajectory Estimation Methodology for Kinematic Laser Scanning. *ISPRS Journal of Photogrammetry and Remote Sensing*, 215, 62–79.

Pöppl, F., Ullrich, A., Mandlburger, G., Pfeifer, N., 2025. Precise and Efficient High-Frequency Trajectory Estimation for LiDAR Georeferencing. *ISPRS Journal of Photogrammetry and Remote Sensing*, 223, 344–361.